ACS APPLIED MATERIALS & INTERFACES

www.acsami.org

Research Article

Functionalized Terpolymer-Brush-Based Biointerface with Improved Antifouling Properties for Ultra-Sensitive Direct Detection of Virus in Crude Clinical Samples

Michala Forinová,[▽] Alina Pilipenco,[▽] Ivana Víšová, N. Scott Lynn, Jr, Jakub Dostálek, Hana Mašková, Václav Hönig, Martin Palus, Martin Selinger, Pavlína Kočová, Filip Dyčka, Jan Štěrba, Milan Houska, Markéta Vrabcová, Petr Horák, Judita Anthi, Chao-Ping Tung, Chung-Ming Yu, Chi-Yung Chen, Yu-Chuan Huang, Pei-Hsun Tsai, Szu-Yu Lin, Hung-Ju Hsu, An-Suei Yang, Alexandr Dejneka, and Hana Vaisocherová-Lísalová*

Cite This: *ACS Appl. Mater. Interfaces* 2021, 13, 60612–60624

Read Online

ACCESS | Metrics & More | Article Recommendations | Supporting Information

ABSTRACT: New analytical techniques that overcome major drawbacks of current routinely used viral infection diagnosis methods, i.e., the long analysis time and laboriousness of real-time reverse-transcription polymerase chain reaction (qRT-PCR) and the insufficient sensitivity of "antigen tests", are urgently needed in the context of SARS-CoV-2 and other highly contagious viruses. Here, we report on an antifouling terpolymer-brush biointerface that enables the rapid and sensitive detection of SARS-CoV-2 in untreated clinical samples. The developed biointerface carries a tailored composition of zwitterionic and non-ionic moieties and allows for the significant improvement of antifouling capabilities when postmodified with biorecognition elements and exposed to complex media. When deployed on a surface of piezoelectric sensor and postmodified with human-cell-expressed antibodies specific to the nucleocapsid (N) protein of SARS-CoV-2, it made possible the quantitative analysis of untreated samples by a direct detection assay format without the need of additional amplification steps. Natively occurring N-protein−vRNA complexes, usually disrupted during the sample pre-treatment steps, were detected in the untreated clinical samples. This biosensor design improved the bioassay sensitivity to a clinically relevant limit of detection of 1.3×10^4 PFU/mL within a detection time of only 20 min. The high specificity toward N-protein-vRNA complexes was validated both by mass spectrometry and qRT-PCR. The performance characteristics were confirmed by qRT-PCR through a comparative study using a set of clinical nasopharyngeal swab samples. We further demonstrate the extraordinary fouling resistance of this biointerface through exposure to other commonly used crude biological samples (including blood plasma, oropharyngeal, stool, and nasopharyngeal swabs), measured via both the surface plasmon resonance and piezoelectric measurements, which highlights the potential to serve as a generic platform for a wide range of biosensing applications.

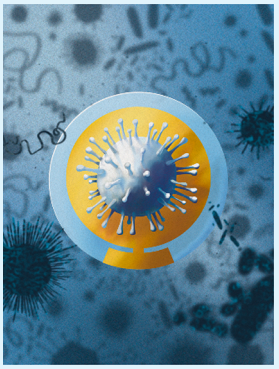

KEYWORDS: *functional coatings, polymer brush, zwitterionic materials, SARS-CoV-2, piezoelectric biosensor, rapid detection*

Downloaded via Jakub Dostalek on January 25, 2022 at 14:34:23 (UTC).
See https://pubs.acs.org/sharingguidelines for options on how to legitimately share published articles.

1. INTRODUCTION

The combination of increasing population density and globalization imposes a challenge to control the spread of infectious diseases, which is well documented by the ongoing coronavirus disease pandemic (COVID-19). To effectively monitor such spreading and to mitigate its impact on the population, there is an urgent need for new, sensitive, rapid, and ideally point-of-care analytical methods. Diagnostic methods can be based on the detection of viral constituents (i.e., viral nucleic acid sequence, proteins) present in clinical samples or, alternatively, may rely on the analysis of an immune response to the infection (i.e., detection of antibodies or other biomarkers). Methods based on the latter, however, are not as useful for rapid diagnostics, as immune responses usually appear several days after the onset of disease symptoms.[1] Severe acute respiratory syndrome coronavirus 2 (SARS-CoV-2), the cause of COVID-19, is an enveloped virus with a genome encoded in the form of positive-sense single-stranded viral ribonucleic acid (vRNA). The virion is primarily composed of four structural proteins: a spike protein (S), an envelope protein (E), a membrane protein (M), and a nucleocapsid protein (N).[2]

Real-time reverse-transcription polymerase chain reaction (qRT-PCR) is the predominant method to diagnose COVID-

Received: September 2, 2021
Accepted: December 2, 2021
Published: December 13, 2021

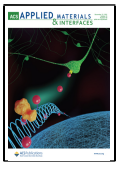

ACS Publications

© 2021 American Chemical Society

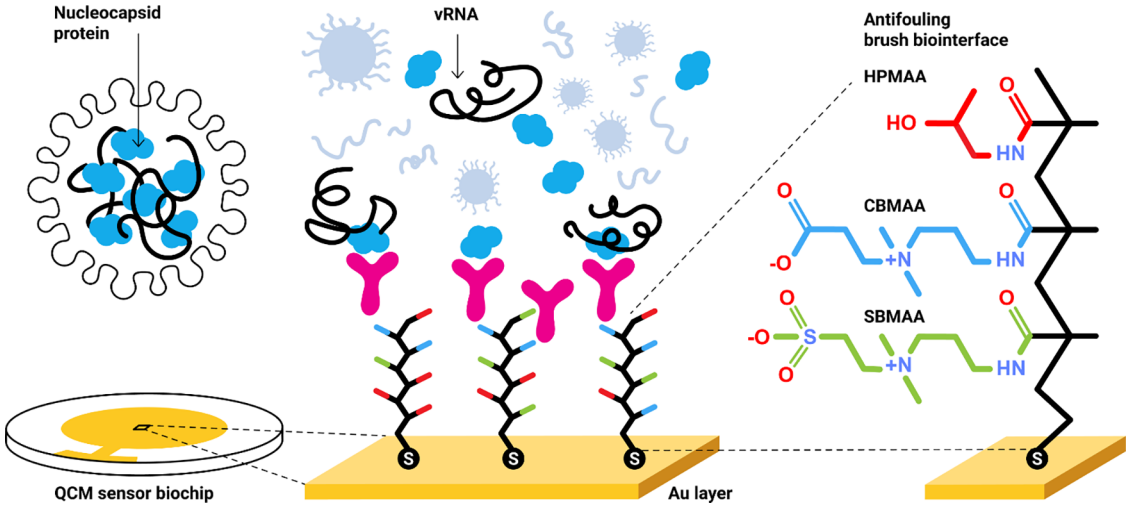

Figure 1. Single-step label-free detection assay scheme based on an antifouling polymer brush biointerface prepared on a gold-coated piezoelectric quartz crystal microbalance (QCM) chip. The antifouling brush biointerface is postmodified with a tailored human-cell-produced antibody specific to SARS-CoV-2 nucleocapsid protein in a complex with vRNA. The antifouling polymer brush architecture is prepared from a random terpolymer of carboxybetaine methacrylamide (CBMAA), *N*-(2-hydroxypropyl) methacrylamide (HPMAA), and sulfobetaine methacrylamide (SBMAA).

19, allowing for the sensitive detection of SARS-CoV-2 vRNA sequences with a limit of detection (LOD) in the range of 10^2–10^4 copies/mL.[3,4] However, its long analysis time (1–3 h) has motivated the development of more rapid vRNA amplification assays, including reverse-transcription loop-mediated isothermal amplification[5] and a variant coupled with clustered regularly interspaced short palindromic repeat-Cas12 lateral flow assay,[6] providing a short analysis time (30 min) with LOD as low as 10 copies/mL. These amplification-based assays, however, require additional sample preparation to isolate the target vRNA from the collected samples, prolonging the time by 30–60 min and further requiring specialized laboratories with trained personnel. Moreover, the increasing complexity of the assay raises the probability of cross-contamination, potentially necessitating a repeat of the assay.

Lateral flow immunoassays, often referred to as antigenic tests, are based on the analysis of structural viral proteins (typically by a sandwich immunoassay format). They provide fast, simple, and cost-efficient detection of SARS-CoV-2;[7] however, they typically only offer a qualitative readout and have significantly decreased sensitivities when compared to qRT-PCR: LODs are up to 10^5 times higher than those achievable by qRT-PCR.[8] Their sensitivities may be further significantly reduced for on-site use due to user errors during the pre-analytical phase. Hence, they do not provide an ideal solution for rapid and reliable screening of COVID-19, and they are better suited in less demanding frontline testing or as a tool suitable only in situations when other methods are not available.[7,9]

The still unmet challenge of both rapid (<30 min, including sample preparation) and highly sensitive (LOD comparable with qRT-PCR) detection of SARS-CoV-2 is currently being addressed by research aimed at various affinity biosensor platforms,[10] including those based on electrochemical,[11−13] field-effect transistor,[14,15] surface plasmon resonance (SPR),[16,17] and fluorescence[17] methods. These methods usually probe the affinity capture of viral constituents after exposure to liquid samples, where each sensor surface is conjugated with biorecognition elements (BREs) specific to SARS-CoV-2 structural proteins (or vRNA sequences). The readout time, sensitivity, and other key analytical characteristics rely heavily on the complexity of the detection format (summarized in Table S1). All of these surface-mediated techniques suffer to a certain extent from the nonspecific binding (fouling) of biomolecules (abundant in complex liquid samples) to the sensing surfaces. Various approaches have been employed to mitigate the detrimental effects of fouling, including the isolation of the target analyte from the complex sample, diluting the sample, blocking the surface with additional molecules (e.g., bovine serum albumin or casein), and washing the surface to remove loosely bound nonspecifically adsorbed biomolecules.[18] These approaches, however, also affect a biosensor's performance as they prolong the readout time, lower the sensitivity and accuracy, and increase the assay complexity.

Remarkable research efforts have been devoted to the development of functional biointerface coatings resistant to fouling (antifouling surfaces) that, when used with surface-based biosensors, allow for the direct detection of target analytes in complex biological media (e.g., undiluted bodily fluids). The molecular foundation of modern functionalizable antifouling coatings is numerous and ranges from ethylene glycol derivatives, (poly)saccharides, and peptides, to more complex moieties formed from various zwitterionic and non-ionic surface structures, including self-assembled monolayers, polymer brushes, hydrogels, and even more complex macromolecular architectures, as also reported in several recent reviews.[19−24]

Surfaces with the highest fouling resistance include those based on polymer brushes, prepared by grafting hydrophilic electroneutral polymers from the surface.[20,25] These include examples of non-ionic poly(2-hydroxyethyl methacrylate), poly(3-hydroxypropyl methacrylate), poly(*N*-isopropyl acrylamide),[26] poly(*N*-(2-hydroxypropyl) methacrylamide) (pHPMAA);[27] and zwitterionic poly(carboxybetaine)-based (pCB) brushes such as poly(carboxybetaine) methacrylate,[28] poly(carboxybetaine methacrylamide) (pCBMAA), poly(carboxybetaine acrylamide) (pCBAA),[29] or copolymer structures combining zwitterionic and non-ionic moieties

https://doi.org/10.1021/acsami.1c16930
ACS Appl. Mater. Interfaces 2021, 13, 60612−60624

such as random p(CBMAA-*co*-HPMAA).[30] The diverse physicochemical surface properties of these structures − including chemical composition, thickness, rigidity, wettability, surface charge, packing density, or swelling properties − have been shown to have a substantial impact on their antifouling properties.[20,31,32]

Regarding the use for biosensors, carboxy-functional zwitterionic pCB brushes have been shown to possess very desirable properties, combining excellent antifouling properties with an ease of functionalization (via amine coupling chemistry, typically using 1-ethyl-3-(3-dimethylaminopropyl)-carbodiimide hydrochloride/*N*-hydroxysuccinimide (EDC/NHS) coupling, Figure S1); these pCB brushes have been increasingly used in various biosensing applications for the sensitive detection of protein biomarkers, microRNAs, and bacterial pathogens present in various complex biological media.[20,24,33,34] However, the chemical reactions involved in pCB functionalization, namely, the conversion of the pCB carboxyl groups to active esters, may result in the undesired presence of residual active esters in the brush. It has been shown that a significant portion of these active esters does not spontaneously hydrolyze back to the original carboxyl groups, inducing surface charge imbalances and changes in the overall brush structure, which significantly impair the antifouling properties of the surface.[33] Several approaches have been proposed to compensate for these effects. One approach involved the covalent attachment of small molecules bearing primary amines and the carboxyl groups, which quench the residual active esters remaining after the surface functionalization.[33] Another approach employs copolymerization of CB with non-functionalized antifouling HPMAA, hence suppressing the associated impairment of the final coating.[27,30] However, none of these approaches can completely recover the fouling resistance of non-functionalized pCB and take into account the physicochemical properties of BREs themselves.

In this study, we present a novel biofunctional polymer brush, based on a terpolymer architecture, that is shown to retain its antifouling properties even after functionalization with BREs. This terpolymer architecture, shown schematically in Figure 1, has a tailored composition that allows (i) minimization of the structural impairment of the brush caused by the functionalization and (ii) effective shielding of possible charge imbalances caused by BRE coupling and BRE presence itself. We demonstrate performance of this biointerface through the rapid, sensitive, and quantitative detection of SARS-CoV-2 constituents directly in crude clinical samples. We show that this biointerface, in combination with a common piezoelectric sensor technique,[35] allows for the direct monitoring of the specific capture of both N-protein and naturally occurring N-protein/vRNA complexes. This work highlights the utmost importance of the functionalizable biosensor antifouling interface, a critical component for the sensitive label-free detection of SARS-CoV-2 in real-world untreated biological samples. Indeed, by avoiding any sample pre-treatment steps, this biosensor takes advantage of the selective capture of natively occurring N-protein−vRNA complexes on the antifouling biointerface, thus significantly increasing the mass detected through the piezoelectric method, eliminating the need for additional signal amplification steps. The key biosensor performance characteristics are determined and confirmed by standard qRT-PCR experiments performed side-by-side on a series of clinical nasopharyngeal swab samples.

2. RESULTS AND DISCUSSION

The biosensor developed herein, shown schematically in Figure 1, relies on an antifouling brush biointerface tailored to SARS-CoV-2 detection that is prepared on a piezoelectric quartz microbalance (QCM) chip. The surface of this chip is postmodified with custom-produced high-affinity antibodies against the N-protein of SARS-CoV-2 (AbN). Crude liquid samples are delivered to the sensor surface in a flow cell by a microfluidic system, where the specific capture of the target analytes is directly monitored in real time via changes in the oscillation frequency f of the piezoelectric quartz crystal.

2.1. Terpolymer Brush Interface. To detect the presence of SARS-CoV-2 virus directly in complex biological fluids, the surface of the piezoelectric QCM chip was chemically modified with the antifouling terpolymer brush. The brush shown schematically in Figure 1 is a random terpolymer of *N*-(2-hydroxypropyl) methacrylamide (HPMAA), carboxybetaine methacrylamide (CBMAA), and sulfobetaine methacrylamide (SBMAA). The dry thickness of the brush was 50 ± 10 nm (for more details on the polymerization and surface characterization, see the Supporting Information and Methods). Each monomer unit in the resulting poly(HPMAA-*co*-CBMAA-*co*-SBMAA) brush coating was chosen to play a specific role: the HPMAA units form a robust non-ionic antifouling background,[30] the zwitterionic CBMAA units provide carboxyl-groups for the conjugation of antibodies, and the SBMAA units carry a permanent negative charge, which, in contrast to the carboxyl group, is independent of pH of the microenvironment.

Immunoglobulin G (IgG) antibodies such as custom-produced antibody against the nucleocapsid protein of SARS-CoV-2 (AbN) can be anchored to the terpolymer chains via their amine groups, which react with active esters on the surface (formed via the carboxyl groups via EDC/NHS coupling, Figure S1) to form amide bonds; more details of the optimized EDC/NHS coupling protocol used herein are illustrated in the Supporting Information. This coupling reaction results in a deficit of negative charges in the CBMAA zwitterionic structure, caused by residual unreacted active esters that did not participate in AbN coupling (Figure S1). These unreacted esters can be deactivated by covalent coupling with glycine or 2-(2-aminoethoxy)acetic acid;[33] however, this deactivation does not proceed to completion, and as a consequence, the original betaine structure is not fully recovered, leading to a deterioration of fouling resistance.

To maintain optimal antifouling properties, we first focused on optimizing the molar composition of SBMAA within the polymer brush biointerface. For this, we performed a series of SPR experiments using biochips prepared with variable SBMAA surface concentration. All the biochips were functionalized with an IgG antibody (of similar type as later used AbN); after which, we measured the levels of surface fouling onto each biochip after exposure to undiluted pooled blood plasma, a model complex biological medium that is commonly used for characterization of fouling resistance.[20,24]

The results presented in Figure 2 (more details in Table S2) demonstrate a pronounced effect of SBMAA content on the brush resistance to fouling from undiluted blood plasma. The optimum amount of SBMAA in the polymerization feed was determined as 3 mol %, and the fouling level for IgG-functionalized terpolymer was 10.9 ng/cm^2. This value is approximately two times lower than that obtained for a

https://doi.org/10.1021/acsami.1c16930
ACS Appl. Mater. Interfaces 2021, 13, 60612−60624

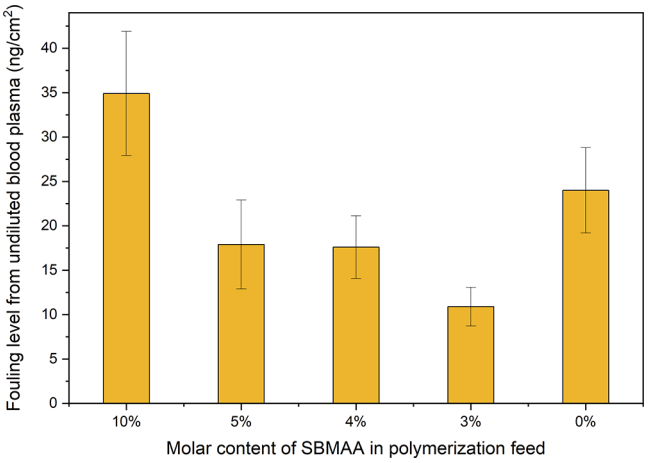

Figure 2. Fouling from undiluted blood plasma on IgG-antibody-functionalized terpolymer brushes prepared by SI-ATRP polymerization using fixed molar content of CBMAA and variable SBMAA content (and consequently HPMAA). Fouling levels were measured by SPR and assessed after 10 min flow of undiluted human blood plasma followed by 10 min rinsing with PBS. The brushes were functionalized with an IgG antibody (anti-*Escherichia coli*) having no natively occurring target in human plasma. The surface mass density of the antibody coupled to the surface was in the range of 150−220 ng/cm^2 for all tested brushes and corresponds approximately to a monolayer.

previously published IgG-functionalized poly(CBMAA-*co*-HPMAA) and even three times lower than for the well-established carboxy-functional zwitterionic antifouling homopolymer brush of pCBAA (see also the Supporting Information, Table S2).

For further biosensor experiments, we fixed the content of CBMAA in the polymerization feed at 20 mol %, as this level provides a sufficient amount of carboxyl groups for the surface postmodification and does not significantly impair the antifouling properties (see Supporting Information Table S2); this content is consistent with previously reported studies on poly(CBMAA-*co*-HPMAA) structures.[30] We further confirmed that the IgG immobilization level is not significantly influenced by SBMAA content in polymerization feed in the range of SBMAA contents of 1−4 mol % (Figure S2). Based on the results shown in Figure 2, we chose to continue with a polymerization feed of 77 mol % of HPMAA, 20 mol % of CBMAA, and 3 mol % of SBMAA for the preparation of the AbN-functionalized antifouling biointerfaces.

It is worth mentioning that the optimum monomer ratio may vary if different types of BREs with distinct physicochemical properties are used. For instance, we observed that for negatively charged DNA oligonucleotide probes anchored to the terpolymer structure, the optimum molar content of SBMAA in the polymerization feed was 0.5 mol % (data not shown). In general, such facile "tuning" capability makes this terpolymer a versatile platform applicable for a broad range of surface chemistry applications. The stability of the terpolymer brush (without the BREs) was verified 45 days after polymerization. No significant changes in its chemical structure were observed when compared to the structure 1 day after polymerization (see infrared spectra presented in Figure S3) proving the long-term stability.

2.2. Specificity of the Custom-Produced Monoclonal Antibody against the SARS-CoV-2 Nucleocapsid Protein.

The biosensor reported herein is based on an antibody specific to SARS-CoV-2 N-protein. This structural protein plays a crucial role in the coronavirus replication cycle,[36] and furthermore, transcriptomic and proteomic studies in both multiple cell culture systems and human clinical samples have shown that it belongs to the abundant viral protein, whereas the surface-exposed S-protein is usually relatively less represented.[37−39] Importantly, current vaccines predominantly target the S-protein of SARS-CoV-2,[40] and it can be assumed that the vaccine-based selection pressure will potentially lead to the occurrence of antibody escape mutants that will complicate the use of antigenic tests specific to S-protein.[41] The alternative whole virus vaccines elicit the antibody response to multiple virus epitopes, making the generation of escape mutants far less probable.[42,43] The stability of the N-protein sequence is, among others, illustrated by the high degree of sequence homology between SARS-CoV-1 and 2 (∼90% similarity of the amino acid sequence).[44] Considering the mutation rate, the SARS-CoV-2 N-protein has been shown to have lower variability than the S-protein.[44] These results thus suggest that the performance of sensors targeting the SARS-CoV-2 N-protein (as that reported herein) will less likely be affected by mutations and new virus variants.

The AbN used in this study was selected from a panel of 46 IgG antibodies based on their performance assessed by immunoblotting (Figure S4) and enzyme-linked immunosorbent assay (ELISA) (data not shown). The specificity of the selected AbN was further tested by immunoblot, which confirmed the binding to N-protein of SARS-CoV-1 and 2 viruses, whereas no binding was observed neither for other human coronavirus N-proteins nor for other common respiratory viruses (Table 1). The observed specificity to both SARS-CoV-1 and 2 (and no other human coronaviruses or other respiratory viruses) might not be a critical issue from the perspective of clinical practice as both viruses are highly pathogenic and the clinical symptoms of the diseases are very similar.

Table 1. Cross-Reactivity of the Selected AbN, Verified with Seven Recombinant Nucleocapsid Proteins from Human Coronaviruses (See Also Figure S5)[a]

coronavirus	result
SARS-CoV-2	POS
SARS-CoV-1	POS
MERS	NEG
229E	NEG
NL63	NEG
OC43	NEG
HKU1	NEG

[a]1 μg/well or 0.1 μg/well nucleocapsid proteins expressed in *Escherichia coli* (*E. coli*) BL21(DE3) separated by SDS-PAGE and electroblotted to a PVDF membrane were reacted with AbN.

2.3. Detection of SARS-CoV-2 Virus by the Piezoelectric Biosensor with the Terpolymer Brush Biointerface.

Piezoelectric QCM biochips having an optimized AbN-functionalized polymer brush architecture were sealed to a flow cell to transport a series of samples containing SARS-CoV-2 over their surface. These samples were prepared from a cell culture medium (solution with a high degree of complexity), whereby for calibration purposes, the virus concentration was determined by a plaque assay. To avoid the potential effects of

https://doi.org/10.1021/acsami.1c16930
ACS Appl. Mater. Interfaces 2021, 13, 60612−60624

viscosity differences on the piezoelectric measurements, both virus-containing samples and the virus-free controls (blank samples) were prepared from cell culture using similar protocols.

Figure 3a shows the typical kinetics of the piezoelectric biosensor signal (f) upon the affinity binding of the SARS-CoV-2 constituents. These sensorgrams were measured for samples with virus concentration ranging between 10^2 and 10^6 PFU/mL; after their contact with the sensor surface, a rapid decrease in f occurs with respect to the baseline established in a working buffer, where f drops to a steady value after a short time (10 min). The surface was then rinsed with working buffer; after which, f increases and (after 5 min) reaches a steady level that is below the original baseline. It can be seen that across all measurements, the sensor response (Δf) increases with the SARS-CoV-2 concentration. Figure 3b displays the respective calibration curve along with a fit obtained using the Sips isotherm (detailed information can be found in Figure S6). From the response to blank samples the $\Delta f_{LOD} = \mu - 3 \times \sigma = -8.5$ Hz was calculated (μ is the average value of frequency change, and σ is the standard deviation value of the blanks), and the biosensor LOD was determined as 1.3×10^4 PFU/mL. Similarly, the limit of quantification (LOQ) was obtained by using the formula $\Delta f_{LOQ} = \mu - 10 \times \sigma$ as 9.1×10^4 PFU/mL. As an additional control, the same QCM biochips were postmodified with a reference IgG antibody (anti-*E. coli*) and tested for the analysis of SARS-CoV-2 samples. As shown in Figure 3b, these biochips showed no detectable sensor response for a concentration of 10^4 PFU/mL.

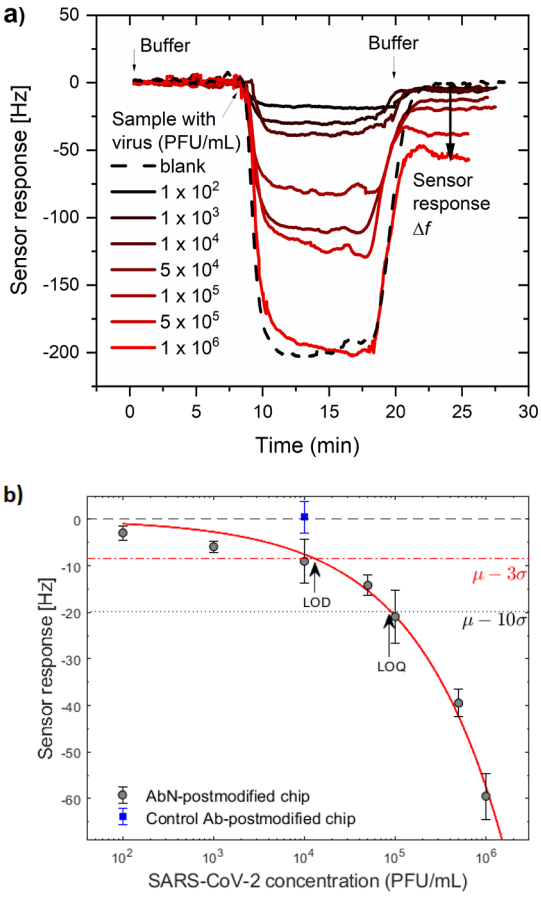

Figure 3. QCM biosensor sensorgrams and calibration curve. (a) Kinetics of the piezoelectric biosensor signal upon the injection of a series of SARS-CoV-2 virus standards prepared from cell culture. (b) Established calibration curve of the piezoelectric biosensor for SARS-CoV-2 detection in a cell culture medium.

The high specificity of these AbN-functionalized interfaces to N-protein binding was verified through the identification of bound proteins from SARS-CoV-2 positive samples by mass spectrometry. Overall, the SARS-CoV-2 nucleocapsid protein was detected as one of the most abundant proteins present, together with subunits of antibodies that were used for N-protein binding (Data S1, Data S2). These results confirm the unique antifouling character of this terpolymer brush biointerface.

However, as no lysis agents, detergents, or other chemicals were used with the cell culture (used in Figure 3), there arises a question on the origin of the observed response of this biosensor that is specific to SARS-CoV-2 N-protein. It is reasonable to assume that the AbN immobilized on the sensor surface cannot directly recognize the SARS-CoV-2 N-protein incorporated within the viral capsid, where it stays hidden from the outside environment. The fact that the sensorgrams in Figure 3 show a strong response to the presence of the virus suggests that the analyzed samples contain both N-protein that is incorporated in the virion structure and N-protein that is outside and originating from the infected cells during virus replication. To confirm this hypothesis, we verified the presence of free N-protein in the medium through gel electrophoresis using the same specific AbN used in the biochip experiments (Figure S7). Interestingly, these data indicate that the majority of the N-protein was recognized in the fraction with the precipitated virions, and concentrations in its free form (which is detected in biosensor experiments) are substantially lower (Figure S7). To further elucidate these observed biosensor binding events, we used qRT-PCR and mass spectrometry to further analyze the deposits that remained bound to the biointerface after conducting the biosensor experiments, in which the SARS-CoV-2-spiked positive controls were employed. The qRT-PCR experiments revealed the presence of vRNA on such biochip surfaces (Table S3), which suggests that vRNA is most likely bound to its natural target, i.e., the N-protein captured on the biochip via specific AbN−N-protein interactions. A more detailed mechanism of this N-protein-vRNA surface-mediated interaction is unclear and will be the subject of our future work. However, these results indicate that biosensor sensitivity may benefit from a lack of sample pre-treatment such as addition of detergents, lysis agents, and other chemical additives, which otherwise disrupt natively occurring biomolecular interactions. In the biosensor platform reported here, the lack of pre-treatment allows biomolecules to occur in the close-to-native form and thus promotes the formation of nucleoprotein complexes that enhances the QCM biosensor response.

2.4. Antifouling Properties of the AbN-Functionalized Terpolymer Brush in Clinically Relevant Samples.

To enable the implementation of this direct assay format for the rapid analysis of SARS-CoV-2 in clinical use, we aimed to minimize the interaction of the abundant constituents of the analyzed clinical samples with the biosensor surface. Such interaction would interfere with the specific recognition of N-protein and native virus constituents' interlinkage. To characterize the antifouling properties of the AbN-functionalized poly(HPMAA-*co*-CBMAA-*co*-SBMAA) terpolymer

https://doi.org/10.1021/acsami.1c16930
ACS Appl. Mater. Interfaces 2021, 13, 60612−60624

brush, we exposed the surface to a set of the most common crude biological samples relevant toward clinical SARS-CoV-2 detection—oropharyngeal, nasopharyngeal, and stool swabs, and swabs from an indoor desk surfaces (all verified as SARS-CoV-2 vRNA-free by qRT-PCR, data not shown). The non-treated extracts from these swabs were collected using a standard protocol and were analyzed directly without pre-treatment.

Following the detection protocol used for the calibration of the developed biosensor (see Figure 3a), the QCM sensor signal was monitored during a 10 min injection of the swabbed sample followed by 5 min rinsing with working buffer. The results are summarized in Table 2; the magnitude of the response Δf was below 6 Hz for all the samples. These results clearly confirmed the superior antifouling properties of the AbN-functionalized terpolymer brush, assuring that there was negligible nonspecific interaction with the constituents of these investigated clinical samples. Additional control experiments were performed with AbN-functionalized brushes during the injection of Hepatitis A virus protein (10 μg/mL, an inactivated viral antigen, predominantly in the form of whole virions) and *E. coli* O157:H7 (10^6 CFU/mL, heat-killed) spiked in buffer. Similar to the swabbed samples, the measured sensor responses were below the LOD regarding measurements in complex cell culture media (Figure 3b), displaying the great potential of this method for use in a variety of clinically relevant complex samples.

Table 2. Antifouling Properties of the AbN-Functionalized Biointerface, Listing the Piezoelectric Sensor Response to Nonspecific Adsorption from Selected Set of Clinically Relevant SARS-CoV-2-Free Swab Samples and Control Analytes (Measured in at Least Two Replicates)

sample type	frequency shift, Δf [Hz ± SD]
nasopharyngeal swab	5.5 ± 0.9
oropharyngeal swab	1.0 ± 1.4
stool swab	1.8 ± 2.6
surface swab	0.9 ± 1.0
Hepatitis A virus protein	2.0 ± 0.8
E. coli	1.7 ± 2.0

2.5. Validation of the Antifouling SARS-CoV-2 Biosensor for Crude Clinical Sample Analysis. We employed this optimized polymeric brush biointerface for the analysis of a set of clinical samples. In a blinded study regime, we tested a series of nasopharyngeal swabs (see Figure 4a) acquired using a standard certified protocol from both SARS-CoV-2 negative and positive patients. These samples were analyzed side-by-side at a clinical diagnostic unit using both the biosensor developed herein as well as a standard qRT-PCR protocol. We tested eight clinical samples, four negative and four positive. The vRNA concentrations measured by qRT-PCR for the positive samples were in the range of 4.1×10^5 to 7.4×10^6 copies/mL, which is above the LOD and LOQ determined above. As shown in Figure 4b, the QCM biosensor correctly identified all positive and negative samples when using a cut-off value of $\Delta f_{LOD} = -8.5$ Hz. We furthermore investigated the possibility of using this biosensor for the quantitative detection of SARS-CoV-2 employing the previously established calibration curve (Figure 3b). These results show only partial agreement with qRT-PCR, which can be ascribed to the fact that qRT-PCR quantifies the number of vRNA copies, whereas the biosensor measurement is based on the detection of the N-protein−vRNA complexes (Table 3). In addition, the observed deviation between the quantitative result of this biosensor and qRT-PCR can also be ascribed to the differences in vRNA and protein production that is either present in the virion capsule or likewise, can be found in a free form outside of the virion capsule.[45]

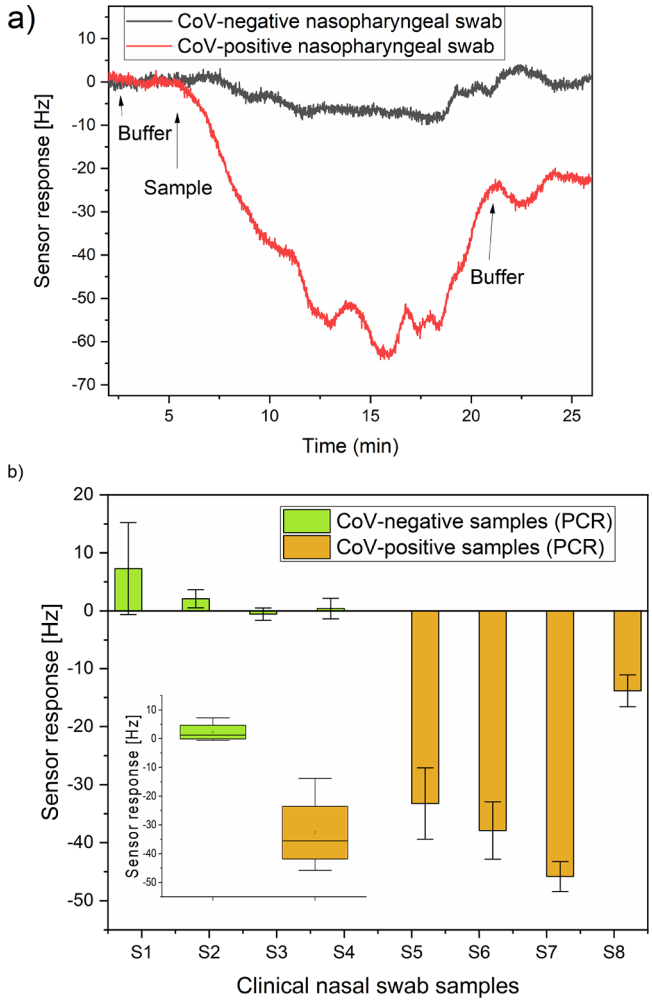

Figure 4. (a) Examples of the real-time response of this antifouling piezoelectric biosensor to clinical samples (i.e., nasopharyngeal swab extracts). (b) Summary of the antifouling biosensor and qRT-PCR-based detection clinical nasopharyngeal swab samples. The difference between the piezoelectric signals for positive and negative clinical samples (qRT-PCR verified) taken from nasopharyngeal swab samples was statistically significant.

Table 3. Comparison of Quantitative SARS-CoV-2 Detection by the Antifouling Biosensor and qRT-PCR[a]

clinical sample	antifouling biosensor response (Hz)	antifouling biosensor virus conc. (PFU/mL)	qRT-PCR RNA conc. (copies/mL)
S5	−33.3 ± 6.2	$(3.2 \pm 0.6) \times 10^5$	$(4.1 \pm 1.2) \times 10^5$
S6	−37.9 ± 4.9	$(4.0 \pm 0.5) \times 10^5$	$(7.4 \pm 3.2) \times 10^6$
S7	−45.8 ± 2.6	$(5.8 \pm 0.3) \times 10^5$	$(1.2 \pm 0.7) \times 10^6$
S8	−13.8 ± 2.7	$(7.8 \pm 1.5) \times 10^4$	$(1.2 \pm 0.6) \times 10^6$

[a]Virion concentration was calculated from the calibration curve shown in Figure 3b. vRNA concentration was calculated as the average concentration of N, RdRp, and E genes.

https://doi.org/10.1021/acsami.1c16930
ACS Appl. Mater. Interfaces 2021, 13, 60612−60624

In regard to the clinical perspective of the results herein, the methods currently used for the detection of SARS-CoV-2 primarily rely on the detection of viral genetic information (vRNA) by means of qRT-PCR and derived techniques,[46] approaches that are considered the gold standard method with high analytical sensitivity and specificity.[47] As recently evidenced, however, when applied for routine diagnostics, the sensitivity of qRT-PCR is often not reached due to its complex multistep protocol.[48,49] In addition, the presence of vRNA does not necessarily prove the presence of a replicating and thus infectious virus. On the one hand, there are multiple reports of individuals with long-term qRT-PCR SARS-CoV-2 positivity in nasopharyngeal swabs,[47,50] yet prolonged RNA shedding has not been associated with the production of infectious viral particles, as described in several studies.[45,51] On the other hand, rare cases of (immunodeficient) patients with long-term production of infectious virus have also been recorded.[52]

An alternative approach for the detection of SARS-CoV-2 is based on the detection of viral proteins, utilized in numerous antigen-based tests. These tests usually have a lower sensitivity (and specificity) compared with qRT-PCR, but they offer the advantage of less demanding operation and possible point-of-care rapid analysis in several minutes.[8,53,54] The approach reported here combines the advantages of the antigen-based approach, which is more closely related to the presence of replicating virus in the sample, with a sensitivity and specificity that is comparable with qRT-PCR. Furthermore, the approach herein does not require specialized laboratory equipment, trained personnel, or lengthy and laborious sample processing (including vRNA isolation), and the complete analysis time is less than 20 min. The selection of the N-protein as a target protein was beneficial for this type of detection, as even after the disintegration of virions, vRNA remains bound to the nucleocapsid protein due to the high affinity between N-protein and vRNA. As we confirmed, vRNA in the form of an N-protein−vRNA complex is bound to the AbN-functionalized biochip surface (see Table S3), which significantly enhances the mass of the attached molecules and thus increases the signal of a piezoelectric sensor.

Unlike a lateral flow antigen test, the biosensor reported here provides a quantitative output that can serve for measurement of the concentration of SARS-CoV-2 nucleocapsid protein. However, it should be noted that the relationship between the sensor response corresponding to binding of N-protein−vRNA complexes and the amount of infectious viral particles might be even more complex as several other factors such as the individual course of infection and host immune response are taking place.[37,38] Furthermore, in line with the results shown in Table 3, a direct comparison between the quantitative data obtained with methods based on vRNA and viral protein detection is limited due to poor correlation between vRNA concentration and protein production.[45]

It should be noted that various other SARS-Cov-2 biosensors have been reported in the literature, including those based on commonly used electrochemical-, optical-, and field-effect transistor-based technologies. As summarized in Table S1, however, the majority of these works do not meet the criteria for rapid and sensitive detection in clinical samples. Typically, biosensors relying on vRNA detection require an additional RNA extraction step in a challenging RNase-free environment[11,55] or other pre-treatment steps, such as purification, dilution, or heating.[56,57] The comparison of LODs between previously reported biosensors is complicated, as the conversion between a great variety of units and sample types is not straightforward. Several biosensors have shown a sensitivity comparable to PCR-based methods. For example, the work on a field-effect transistor biosensor has reported an LOD of 1.6×10^1 PFU/mL of cultured virus and 2.42×10^2 copies/mL in clinical samples (albeit working with heat-inactivated samples).[14] Another electrochemical biosensor based on the sandwich assay and a 30 min incubation time, functionalized with antibodies targeting S- or N-protein, has reported LODs of 6.5 PFU/mL and 6.5×10^3 PFU/mL, respectively (but relying on a complex assay format).[58] The LOD of the piezoelectric biosensor reported herein is 1.3×10^4 PFU/mL, higher than both of these works. Nevertheless, even at this level, it was capable of correctly identifying CoV-positive patients with the advantage of an extremely simple direct detection format that allows overcoming of complex sample pre-treatment steps.

3. CONCLUSIONS

The combination of interdisciplinary research in the area of surface chemistry, bioengineering, and virology has paved the way to herein reported highly sensitive method for rapid detection of respiratory viruses in real-world samples. It takes advantage of a tailored biointerface, optimized for AbN bioreceptors, which significantly reduces the nonspecific adsorption from complex biological samples relevant to COVID-19 diagnosis. The key advantages it can offer is the possibility of rapid direct analysis of untreated clinical samples with a sensitivity comparable with qRT-PCR. In addition, the deploying of the antifouling biofunctional interface at a QCM-based transducer gives the opportunity for quantitative characterization of the concentration of viral constituents. These features may have a critical impact for use in clinics for precise COVID-19 diagnosis, as well as in disease prognosis or individual infectivity characterization. The overall characteristics of the developed antifouling biosensor are superior to current state-of-art SARS-CoV-2 detection methods. The observed findings go beyond the "single case of SARS-CoV-2" and may open a new route to biointerface science and detection strategies.

4. METHODS

4.1. Preparation of Terpolymer Brushes. Terpolymer brush coatings were prepared using a modified procedure as described previously.[59] Briefly, 10 MHz gold-coated quartz crystals (Krystaly, Hradec Králové, Czech Republic) or gold-coated SPR chips were cleaned in UV-ozone for 10 min and then were rinsed with ultrapure water (18.0 MΩ.cm, Milli-Q system, Merck) and ethanol (Sigma-Aldrich, Germany). The slides were then immediately immersed in an initiator solution of a 1 mM ω-mercaptoundecyl bromoisobutyrate (ProChimia Surfaces, Poland) in ethanol to form a self-assembled monolayer (SAM) and were left in solution for 3 days at room temperature in the dark. Methanol (Sigma-Aldrich, Germany) and water were degassed via 6 freeze-pump-thaw cycles. For the preparation of 80 coatings, the catalyst solution was prepared as follows: under a nitrogen atmosphere, CuCl (14.9 mM) (Sigma-Aldrich, Germany), $CuCl_2$ (3.3 mM) (Sigma-Aldrich, Germany), and 1,4,8,11-tetramethyl-1,4,8,11-tetraazacyclotetradecane (19.9 mM) (Sigma-Aldrich, Germany) were mixed in a Schlenk tube with degassed methanol. The mixture was sonicated for 5 min to dissolve all solids. In a second Schlenk tube, SBMAA (X = 10, 5, 4, 3, 2, 1, or 0 mol %) (Specific Polymers, France), carboxybetaine methacrylamide - CBMAA (Y = 15 or 20 mol %) (Specific Polymers, France), and HPMAA (Z = 100 − (Y + Z) mol %) (Specific Polymers, France)

https://doi.org/10.1021/acsami.1c16930
ACS Appl. Mater. Interfaces 2021, 13, 60612−60624

monomers were dissolved in degassed water and degassed methanol and stirred. After the dissolution was completed, the catalyst solution was added to the monomer solution using a gastight syringe, so the final ratio of methanol:water is 4:1. The polymerization mixture was added into a reactor containing the substrates coated with the initiator SAM. Polymerization was carried out for 2 h at room temperature. Finally, the samples were washed with ultrapure water and stored in phosphate-buffered saline (PBS, 0.01 M sodium phosphate, 0.138 M sodium chloride, 0.0027 M potassium chloride, pH 7.4) (Sigma-Aldrich, Germany) at 6 °C until use. Verification of the presence of all three monomers was performed using infrared spectroscopy (Figure S3a,b).

4.2. Characterization of Terpolymer Brushes by Spectroscopic Ellipsometry. The thickness of the terpolymer brush was measured using spectroscopic ellipsometry according to a previously described procedure.[59] Gold-coated SPR chips with a terpolymer structure were rinsed with ultrapure water, dried by a flow of nitrogen, and mounted into a spectroscopic ellipsometer (VASE, J.A. Woollam, Lincoln, USA). After system alignment, the spectra in a range of 1−3.8 eV for 3 angles of incidence (65°, 70°, and 75°) were taken. For data analysis, WVASE32 software was used. The model BK7 glass/Ti/Au/polymer layer was built using tabulated optical constants for BK7 glass, and the Ti and Au layer constants were assessed by ellipsometric measurements of a reference bare surface; for the polymer layer, a single-oscillator model was used (Gaussian oscillator). The dry thicknesses of the prepared coatings were in a range of 40−60 nm. Figure S8 shows a typical ellipsometric fit for one embodiment of the terpolymer brush.

4.3. Characterization of Terpolymer Brushes by SPR (Fouling Measurements). SPR chips coated with terpolymer brushes of different composition were rinsed with ultrapure water, dried with a flow of nitrogen, and mounted into a SPR sensor (angular multiparametric SPR with a 4-channel microfluidic system and 785 nm laser source, BioNavis Ltd., Finland). For fouling measurements on the bare non-activated surface, a baseline in PBS (30 μL/min, 10 min) was established. Undiluted blood plasma was then injected (30 μL/min, 10 min), followed by PBS (30 μL/min, 10 min), higher ionic strength PBS-NaCl (0.01-M phosphate, 0.75-M sodium chloride, 0.0027-M potassium chloride, pH 7.4) (30 μL/min, 5 min), and PBS (30 μL/min, 10 min). The fouling level was assessed as the difference between the SPR sensor baselines in the PBS before the plasma injection and both before and after the 5 min rinse with PBS-NaCl (as indicated in the data).

For the fouling level measurements of the functionalized surfaces, IgG polyclonal antibodies against *E. coli* O157:H7 were immobilized as follows. SPR chips coated with terpolymer brushes of different composition were rinsed with ultrapure water, dried with a flow of nitrogen, and mounted into SPR. Thereafter, an aqueous solution of EDC/NHS (0.5 M EDC + 0.1 M NHS) was injected (12 μL/min, 20 min), followed by injections of ultrapure water (2 min), 50 μg/mL of anti-*E. coli* antibody (KPL Inc., USA) in HEPES buffer (5 mM HEPES buffer, pH 7, 15 μL/min, 20 min), and water (2 min). The deactivation was performed using an aqueous solution of 1 M 2-(2-aminoethoxy)acetic (AlfaAesar, Germany) acid (12 μL/min, 25 min). Subsequently, ultrapure water (2 min, 30 μL/min) and PBS (10 min, 30 μL/min) were injected to create a baseline. These experiments then continued according to the same procedure as described for the bare non-activated surfaces above.

We used a factor (0.001° = 0.85 ng/cm^2) for the conversion of the SPR sensor response in angular units into surface mass density units. The presented data are the average from the data obtained after performing at least three experiments.

4.4. Production of the Seven Human Coronavirus Nucleocapsid Proteins. The seven human coronavirus nucleocapsid protein genes were derived from the NCBI protein databank. These proteins were codon optimized and synthesized for expression in *E. coli* and mammalian cells in pET15b (Novagen, USA) and pcDNA3.1 (Thermo Fisher Scientific, USA) vectors, respectively. These coronavirus N-protein constructs with a pET15b vector were overexpressed in *E. coli* BL21 (DE3) cells with 0.5 mM IPTG induction at 16 °C. The recombinant coronavirus N-proteins were purified using Ni^{2+}-charged Chelating Sepharose FF (for His-tag binding) with A (binding) buffer containing 50 mM Tris−HCl, pH 8.0 and 600 mM NaCl (Lach-ner, Czech Republic), and B (elution) buffer containing 50 mM Tris−HCl, pH 8.0, 600 mM NaCl, and 500 mM imidazole using an ÄKTAprime plus chromatography system (Cytiva, UK). The fractions containing coronavirus N-proteins were pooled for size exclusion separation with Superose 12 10/300 GL columns (Cytiva, UK) and elution buffer containing 50 mM Tris, pH 8.0, and 600 mM NaCl. For HKU1 N-protein preparation, the NaCl concentration was increased to 1 M to prevent protein precipitation. Purification of the coronaviral N-proteins was confirmed by SDS-PAGE (Figure S9), and proteins were further stored at −20 °C in aliquots.

4.5. Characterization of the IgG1s Derived from the Selection and Screening Procedure with Phage-Displayed Synthetic Single Chain Variable Fragment Libraries. The construction and characterization of the phage-displayed synthetic scFv libraries followed the same procedure, without modification, as described previously.[60] The experimental procedures for panning the phage display libraries, selecting and screening of phage-displayed scFv binders, characterizing the scFvs binding to the cognate antigens and Protein A/L with ELISA, reformatting scFvs into IgG1s, expressing in and purifying IgG1s, and determining EC50 for the antibody−antigen interaction with ELISA have been described in previous works.[60−63]

4.6. Construction and Expression of IgG. VH and VL DNA fragments were separately PCR amplified. The VH and VL DNA fragments were assembled into the plasmid for IgG1 expression with the pIgG expression system (U.S. patent no. 5,736,137) using the Gibson assembly cloning kit (NEB Cat no. E5510S, USA). IgGs were expressed by Expi293 cells following the manufacturer's instruction manual and purified through protein A column, eluted with 0.2 M glycine/HCl buffer, pH 2.5, and neutralized with 1 M Tris buffer, pH 9.0.

4.7. IgG Binding to N-Protein from Transfected 293 T Cells. pcDNA3.1-SARS-CoV-2-N-His was transfected into HEK 293 T cells by transient transfection using ExpiFectamine (Gibco, USA), and cells were seeded into 96-well plates (Thermo Fisher Scientific, USA) at a density of 6 × 106 cells/100 μL/well and cultured for 48 h. After the removal of medium, cells were fixed with 200 μL/well of fixation reagent (methanol:acetone (1:1)) for 10 min at room temperature (RT). After the removal of the fixation reagent and air-drying for 10 min at RT, cells were rinsed with 200 μL of PBS, 100 μL of 0.5% Triton X-100 in PBS was added to each well, and incubated for 5 min at RT to permeabilize the cell membranes. Cells were then rinsed three times with 200 μL of PBS and blocked with 5% skimmed milk in PBS-T for 1 h at RT. Immunostaining was performed with AbN (1 μg/100 μL in PBS-T) as the primary antibody for 2 h at RT, washed twice with PBS-T, and diluted (1:5000) HRP-conjugated anti-human IgG Fc (A80-304P, Bethyl Laboratories, USA) was applied as the secondary antibody for 1 h at RT. After two washes with PBS-T, a signal was developed by adding 100 μL/well of ready-to-use TMB (ScyTek Laboratories, Inc., USA) for 5 min, and the reaction was stopped by 1 N HCl (100 μL per well). Absorbance was measured at 450 nm (Figure S9).

4.8. Virus and Cell Culture. Virus infection experiments were performed in a biosafety level 3 laboratory. SARS-CoV-2 (SARS-CoV-2/human/Czech Republic/951/2020, EPI_ISL_414477, isolated from a clinical sample at The National Institute of Public Health Centre for Epidemiology and Microbiology, Prague, Czech Republic), kindly provided by Dr. Jan Weber, Institute of Organic Chemistry and Biochemistry, Prague, Czech Republic, was passaged in Vero E6 cells (African green monkey kidney cells, ATCC CRL-1586) up to six times before its use in this study. Vero E6 cells were cultured at 37 °C and 5% CO_2 in DMEM low glucose (Biosera, France) supplemented with 10% fetal bovine serum (Biosera, France), 1% L-glutamine (Biowest, France), 100 U/mL penicillin (Biowest, France), 100 μg/mL streptomycin (Biowest, France), and 0.25 μg/mL amphotericin B (Biowest, France). To produce high titre viral stocks, we used 100

https://doi.org/10.1021/acsami.1c16930
ACS Appl. Mater. Interfaces 2021, 13, 60612−60624

kDa Amicon Ultra-15 Centrifugal Filter Unit (Merck Millipore, Germany) followed by filtration of the concentrated viral suspension through a 0.22 μm filter (VWR, USA). The titre of the virus was measured by the plaque assay (see below). The virus was then diluted in cultivation media as required for further experiments.

4.9. Plaque Assay. Plaque assays were performed as previously described with slight modifications.[64] Suspension cultures of Vero E6 cells were seeded (1.3×10^5 cells per well) to a 24-well tissue culture plate with 10-fold dilutions of virus. After 4 h of incubation at 37 °C with 5% CO_2, each well was overlaid by a complete medium with 1.5% carboxymethylcellulose. After a 5 day incubation at 37 °C and 5% CO_2, cell monolayers were stained using naphthalene black. Viral titres were expressed as plaque-forming units (PFU) per milliliter.

4.10. Clinical and Surface Swab Samples. Oropharyngeal, nasopharyngeal, stool, and throat swabs were collected in native conditions according to a standard sampling WHO-approved protocol. Nasopharyngeal swabs infected with SARS-CoV-2 were taken from symptomatic patients. Surface samples were taken from an indoor table; the surface (with an area 225 cm^2) was wiped for 30 s. After addition of 1 mL of PBS, the samples were vortexed, incubated for 5 min at room temperature, and the whole volume was transferred into a microtube. All swabs were collected with certified swab kits. All samples were obtained in accordance with the Ethical Commission's regulations and with a release of informed consent.

4.11. RNA Extraction and qRT-PCR for SARS-CoV-2. RNA was extracted from 200 μL of samples with the Nucleic Acid Extraction Kit B-200 (Zybio, China) using a nucleic acid isolation system (Zybio EXM3000, China). qRT-PCR was performed using the Seegene AllPlexTM 2019-nCoV Assay kit (Seegene, South Korea) in the CFX96 Touch Real-time PCR Detection cycler System (Bio-Rad, USA). Evaluation of the data was performed on the basis of the manufacturer's manual using the CFX Maestro software (Bio-Rad, USA). A similar procedure was used for detection of SARS-CoV-2 vRNA bound to biochips (n = 12), with RNA released to 200 μL of PBS from the biochips by heating the samples at 70 °C for 5 min (Table S3).

4.12. Functionalization of the Polymeric Brush. For both biochip functionalization and real-time detection, we used the openQCM Q-1 (Novaetech, Italy) with an associated microfluidic system. Prior to starting the QCM experiment (constant ambient temperature), the system was temperature-stabilized according to the manufacturer's recommendations. All solutions were degassed before use, reducing the potential of spontaneous bubble formation; if bubbles were present during an experiment, detectable both visually as well as by large increases in f, the experimental data was discarded. Coatings were first rinsed with ultrapure water, mounted to the sensor, washed with PBS buffer for 5 min at a flow rate of 45 μL/min, and finally washed with ultrapure water for 5 min at the same flow rate. For functionalization, brushes were activated with a freshly prepared solution of 0.1 M *N*-hydroxysuccinimide (NHS) and 0.5 M *N*-ethyl-*N*′-(3-diethylaminopropyl)carbodiimide (EDC) (Cytiva, Sweden) for 20 min (7 μL/min). Afterward, the coatings were washed for 3 min (60 μL/min) with 4-(2-hydroxyethyl)-1-piperazine ethanesulfonic acid (HEPES) (5 mM, pH 6.0) (Sigma-Aldrich, Germany). A solution of AbN in HEPES buffer (5 mM, pH 7.0) was injected at a flow rate of 60 μL/min for 1 min; after which, the flow rate was gradually reduced to 15 μL/min over a period of 12 min. After functionalization, all coatings were rinsed with HEPES buffer (5 mM, pH 6.0, 10 min, 30 μL/min) and treated with a deactivation solution of 1 M 2-(2-aminoethoxy)acetic acid (AlfaAesar, Germany) (25 min at a flow rate of 7 μL/min). Deactivated coatings with immobilized antibodies were used for the detection of SARS-CoV-2 virus in the next step.

4.13. Detection of SARS-CoV-2 Virus by the Antifouling Piezoelectric Biosensor. The real-time detection of SARS-CoV-2 virus proceeded using biochips with immobilized AbN from the previous step. A flow rate of 30 μL/min was used to create a stable baseline. Coatings were then rinsed with PBS buffer for 10 min; after which, the sample was injected and left to react for 10 min. Finally, all coatings were rinsed with PBS buffer for 10 min. The amount of detected SARS-CoV-2 virus was calculated from the sensor response in PBS buffer before and after the application of the sample. Detection assays of Hepatitis A virus protein inactivated with formaldehyde (Abbexa, UK) and heat-killed *E. coli* O157:H7 (SeraCare, USA) were performed by same method.

4.14. Precipitation of SARS-CoV-2 Using PEG6000. Virus particles were precipitated from 1 mL of growth medium from Vero E6 cells infected with SARS-CoV-2 using PEG6000.[65] The medium was centrifuged at 5000 × g for 10 min, and 20 g/L NaCl was added to the supernatant together with 50% PEG6000 (Sigma Aldrich, Germany) in 0.5 M NaCl (final concentration of PEG6000 8%). The mixture was incubated overnight at 4 °C and was centrifuged the next day at 7000 × g (4 °C, 15 min). Virions in the pellet were resuspended in 1 mL of PBS, and both the virions and the virion-free supernatant were separately precipitated using methanol/chloroform (Lach-ner, Czech Republic).[66] The resulting protein pellets were resuspended in 1 mL of PBS, ensuring that the volumes of the resulting virion-containing and virion-free samples were the same as the volume of the original medium. A similar procedure was performed with medium from uninfected Vero E6 cells (negative controls).

4.15. Immunodetection of SARS-CoV-2 N-Protein by Western Blot. A reducing Laemmli sample buffer (AppliChem GmbH, Germany) was added to the protein samples, and the resulting mixtures were boiled for 5 min and loaded onto a 12% SDS-PAGE gel together with prestained protein marker VI (10−245 kDa, Applichem, Germany). Electrophoresis was performed in a Mini-Protean Tetra Cell (Bio-Rad, USA). The separated proteins were transferred to a PVDF membrane (Cytiva, UK) for 1 h at 20 V by semi-dry transfer in TRANS-BLOT SD (Bio-Rad, USA). The membrane was blocked (5% skimmed milk in PBS-T (Sigma Aldrich, Germany)) and incubated with anti-SARS-CoV-2 AbN, and subsequently with a secondary antibody conjugated with HRP (VectorLabs, USA). Between each incubation step, the membranes were washed three times in PBS-T. The chemiluminescent signal was developed using the WesternBright Quantum kit for horseradish peroxidase (Advansta, USA). The images of gels and membranes were captured and digitalized using the G:BOX Chemi XX6 system (Syngene, UK).

4.16. NanoLC−ESI−MS/MS Identification of Biochip-Bound Proteins. Proteins bound to the biochip were identified after solution-based trypsin digestion by mass spectrometry. Seven biochips with immobilized antibody were exposed to positive samples (10^4 PFU/mL) by the same procedure described in the section Detection of SARS-CoV-2 Virus by the Antifouling Piezoelectric Biosensor. For a negative control, we used a biochip simply subjected to an activation/deactivation procedure using biochips without immobilized AbN on the surface. Protein digestion was performed directly on the biochip by addition of 200 μL of 12.5 ng/μL trypsin and overnight incubation at 37 °C. The digestion was terminated by the addition of formic acid to a final concentration of 5%. The obtained peptide mixture was purified using C18 Empore disks (3 M, USA).[67] Peptides were dissolved in 30 μL of 3% acetonitrile/0.1% formic acid. The analysis was carried out on an UltiMate 3000 RLSCnano system (Thermo Fisher Scientific, USA) coupled on-line to mass spectrometer timsTOF Pro (Bruker Daltonics, Germany). Peptide solution of 2 μL was injected onto an Acclaim PepMap 100 C18 trapping column (300 μm i.d., 5 mm length, particle size 5 μm, pore size 100 Å; Thermo Fisher Scientific) at a 2.5 μL/min flow rate. Bound peptides were eluted from a trapping column onto an Acclaim PepMap 100 C18 analytical column (75 μm i.d., 150 mm length, particle size 2 μm, pore size 100 Å; Thermo Fisher Scientific) and separated by a 48 min long linear gradient of 5−35% acetonitrile/0.1% formic acid at a constant rate of 0.3 μL/min. The column oven temperature was set to 35 °C. The MS analysis was operated in PASEF scan mode with positive polarity. Electrospray ionization was performed using a CaptiveSpray (Bruker Daltonics, Gemany) with capillary voltage at 1500 V, dry gas at 3 L/min, and dry temperature at 180 °C. Ions were accumulated for 100 ms, and 10 PASEF MS/MS scans were acquired per topN acquisition cycle. An ion mobility range (1/K0) was set at 0.6−1.6 Vs/cm^2. Mass spectra were collected over a

https://doi.org/10.1021/acsami.1c16930
ACS Appl. Mater. Interfaces 2021, 13, 60612−60624

m/z range of 100 to 1700. Polygon filtering was applied to exclude the low m/z of singly charged ions. The target intensity was set to 20,000 to repeatedly select the precursor for PASEF MS/MS repetitions. The precursors that reached the target intensity were than excluded for 0.4 min. Collision energies were changed from 20 to 59 eV in 5 steps of equal width between 0.6 and 1.6 Vs/cm^2 of $1/K_0$ values.

Raw MS data were processed by MaxQuant software (version 1.6.14) with integrated Andromeda search engine;[68] the *Homo sapiens* database was downloaded from Uniprot (07. 05. 2021). We used the severe acute respiratory syndrome coronavirus 2 from Uniprot (06. 05. 2021) and the contaminant database included in the MaxQuant software to identify proteins. The default parameters for TIMS-DDA search type and Bruker TIMS instrument were applied. Trypsin/P was set as enzyme allowing up to two missed cleavages in specific digestion mode, the carbamidomethylation of cysteine was used as fixed modification, methionine oxidation and protein N-term acetylation were set as variable modifications, and the minimum required peptide length was set to five amino acids. Precursor ion tolerance was set at 20 and 10 ppm in the first and main peptide search, respectively; the mass tolerance for MS/MS fragment ions was set at 40 ppm; peptide spectrum match (PSM) and protein identifications were filtered using a target-decoy approach at a false discovery rate (FDR) of 1%. Label-free quantification (LFQ) of proteins was done using the algorithm integrated into MaxQuant with minimum ratio count set at 2. Protein data tables obtained from MaxQuant were analyzed using Perseus software (version 1.6.14.0) as well as scripts written in Python 3.8.5.[69] Protein hits to the reverse database, contaminants, and protein only identified with modified peptides were excluded from further analysis. LFQ intensities were transformed by log2.

4.17. Statistical Analysis. Data obtained from the independent piezoelectric QCM biosensor measured as a change in the resonant frequency are presented as the mean ± standard error of the mean. The LOD was calculated from the calibration curve using $\Delta f_{LOD} = \mu - 3 \times \sigma$, where μ is the average value of QCM frequency change caused by the interaction with the virus-free samples (blanks) and σ is the standard deviation value of the blanks. The LOQ was calculated using the formula $\Delta f_{LOQ} = \mu - 10 \times \sigma$. The data in Figure 3b is a filtered representation of the raw-output, calculated via a moving average filter (size window 150, ~1.5 min) with a preservation of the high frequency noise. The data were processed in OriginPro (OriginLab Corporation, USA) and MATLAB (MathWorks, USA).

■ ASSOCIATED CONTENT

Supporting Information

The Supporting Information is available free of charge at https://pubs.acs.org/doi/10.1021/acsami.1c16930.

Summary of the analytical features of SARS-CoV-2 biosensors in the literature (Table S1); Optimization of terpolymer composition (Table S2); qRT-PCR detection of SARS-CoV-2 vRNA on biochips (Table S3); The general course of EDC/NHS chemistry used for BRE conjugation (Figure S1); Level of immobilization (Figure S2); FT-IRRAS spectra of poly[HPMAA-CBMAA-SBMAA] (Figure S3); Detection of recombinant N proteins with immunoblotting (Figure S4); SDS-PAGE analysis of purified coronavirus N proteins (Figure S5); Best fit isotherms to the calibration data (Figure S6); Immunodetection of nucleocapsid protein N by SDS-PAGE and immunoblotting (Figure S7); An example of the ellipsometric data measured for terpolymer structures to assessed dry thickness (Figure S8); SARS-CoV-2 N protein detection in transfected HEK293T cells (Figure S9) (PDF)

LFQ representation as a heatmap for the most abundant proteins identified after trypsin digestion by nanoLC−ESI−MS/MS (Data S1) (PDF)

The most abundant proteins identified after trypsin digestion by nanoLC−ESI−MS/MS (Data S2) (XLS)

■ AUTHOR INFORMATION

Corresponding Author

Hana Vaisocherová-Lísalová − *Institute of Physics of the Czech Academy of Sciences, 182 21 Prague, Czech Republic;* orcid.org/0000-0002-8755-2398; Phone: +420 266 05 29 93; Email: lisalova@fzu.cz

Authors

Michala Forinová − *Institute of Physics of the Czech Academy of Sciences, 182 21 Prague, Czech Republic*

Alina Pilipenco − *Institute of Physics of the Czech Academy of Sciences, 182 21 Prague, Czech Republic;* orcid.org/0000-0002-3059-6314

Ivana Víšová − *Institute of Physics of the Czech Academy of Sciences, 182 21 Prague, Czech Republic*

N. Scott Lynn, Jr − *Institute of Physics of the Czech Academy of Sciences, 182 21 Prague, Czech Republic*

Jakub Dostálek − *Institute of Physics of the Czech Academy of Sciences, 182 21 Prague, Czech Republic; Austrian Institute of Technology GmbH, 3430 Tulln, Austria;* orcid.org/0000-0002-0431-2170

Hana Mašková − *Faculty of Science, University of South Bohemia, 370 05 České Budějovice, Czech Republic*

Václav Hönig − *Institute of Parasitology, Biology Centre CAS, 370 05 České Budějovice, Czech Republic; Veterinary Research Institute, 621 00 Brno, Czech Republic*

Martin Palus − *Institute of Parasitology, Biology Centre CAS, 370 05 České Budějovice, Czech Republic; Veterinary Research Institute, 621 00 Brno, Czech Republic*

Martin Selinger − *Faculty of Science, University of South Bohemia, 370 05 České Budějovice, Czech Republic; Institute of Parasitology, Biology Centre CAS, 370 05 České Budějovice, Czech Republic*

Pavlína Kočová − *Faculty of Science, University of South Bohemia, 370 05 České Budějovice, Czech Republic*

Filip Dyčka − *Faculty of Science, University of South Bohemia, 370 05 České Budějovice, Czech Republic*

Jan Štěrba − *Faculty of Science, University of South Bohemia, 370 05 České Budějovice, Czech Republic*

Milan Houska − *Institute of Physics of the Czech Academy of Sciences, 182 21 Prague, Czech Republic*

Markéta Vrabcová − *Institute of Physics of the Czech Academy of Sciences, 182 21 Prague, Czech Republic*

Petr Horák − *Institute of Physics of the Czech Academy of Sciences, 182 21 Prague, Czech Republic*

Judita Anthi − *Institute of Physics of the Czech Academy of Sciences, 182 21 Prague, Czech Republic*

Chao-Ping Tung − *Genomics Research Center, Academia Sinica, Taipei 115, Taiwan*

Chung-Ming Yu − *Genomics Research Center, Academia Sinica, Taipei 115, Taiwan*

Chi-Yung Chen − *Genomics Research Center, Academia Sinica, Taipei 115, Taiwan*

Yu-Chuan Huang − *Genomics Research Center, Academia Sinica, Taipei 115, Taiwan*

Pei-Hsun Tsai − *Genomics Research Center, Academia Sinica, Taipei 115, Taiwan*

Szu-Yu Lin − *Genomics Research Center, Academia Sinica, Taipei 115, Taiwan*

Hung-Ju Hsu − *Genomics Research Center, Academia Sinica, Taipei 115, Taiwan*
An-Suei Yang − *Genomics Research Center, Academia Sinica, Taipei 115, Taiwan*
Alexandr Dejneka − *Institute of Physics of the Czech Academy of Sciences, 182 21 Prague, Czech Republic;* orcid.org/0000-0002-5116-8781

Complete contact information is available at: https://pubs.acs.org/10.1021/acsami.1c16930

Author Contributions

[∇]M.F. and A.P. contributed equally to the work.

Author Contributions

Michala Forinová: Carried out bioanalytical experiments, wrote an original draft of the manuscript; Alina Pilipenco: Carried out the bioanalytical experiments, co-wrote an original draft of the manuscript; Ivana Víšová: Carried out the bioanalytical and surface characterization experiments, reviewing and editing, N. Scott Lynn Jr.: Contributed to data analysis, reviewing and editing; Jakub Dostálek: Reviewing and editing, conceptualization; Hana Mašková: Carried out the molecular biology experiments; Václav Hönig: Carried out the biology research, writing the original draft; Martin Palus: Carried out the biology research, writing the original draft; Martin Selinger: Carried out the molecular biology experiments; Pavlina Kočová: Carried out the molecular biology experiments; Filip Dyčka: Carried out the mass spectrometry research, data analysis; Jan Štěrba: Writing draft of the manuscript, reviewing and editing, conceptualization; Milan Houska: Carried out the biosurface characterization, data analysis; Markéta Vrabcová: Carried out the polymer brush synthesis and characterization; Petr Horák: Data analysis; Judita Anthi: Contributed to surface characterization experiments, reviewing and editing; Chao-Ping Tung: Carried out the molecular biology and bioengineering experiments; Chung-Ming Yu: Carried out the molecular biology and bioengineering experiments; Chi-Yung Chen: Carried out the molecular biology and bioengineering experiments; Yu-Chuan Huang: Carried out molecular biology and bioengineering experiments; Pei-Hsun Tsai: Carried out the molecular biology and bioengineering experiments; Szu-Yu Lin: Carried out the molecular biology and bioengineering experiments; Hung-Ju Hsu: Carried out the molecular biology and bioengineering experiments; An-Suei Yang: Molecular biology research supervision, coordination, reviewing and editing; Alexandr Dejneka: Supervision, coordination; Hana Vaisocherová-Lísalová: Data analysis, review and editing, supervision, conceptualization, coordination.

Funding

This work was supported by the Praemium Lumina quaeruntur of the Czech Academy of Sciences (LQ100101902), by the Czech Science Foundation (contract # P205/ 21-19779S), and by ESIF and MEYS (Project "FZU researchers, technical and administrative staff mobility" — CZ.02.2.69/0.0/0.0/18_053/0016627).

Notes

The authors declare no competing financial interest.

■ ACKNOWLEDGMENTS

The authors would like to thank Jan Weber, Institute of Organic Chemistry and Biochemistry, Prague, Czech Republic, for the provision of the SARS-CoV-2 coronavirus isolate (strain SARS-CoV-2/human/Czech Republic/951/2020, isolated from a clinical sample at the National Institute of Public Health, Prague) and to Petra Straková, Veterinary Research Institute, Brno, Czech Republic, for the propagation of the original amount of the SARS-CoV-2 coronavirus. The authors would like to thank Daniel Špaček for his help with the graphic design.

■ REFERENCES

(1) Hueston, L.; Kok, J.; Guibone, A.; McDonald, D.; Hone, G.; Goodwin, J.; Carter, I.; Basile, K.; Sandaradura, I.; Maddocks, S.; Sintchenko, V.; Gilroy, N.; Chen, S.; Dwyer, D. E.; O'Sullivan, M. V. N. The Antibody Response to SARS-CoV-2 Infection. *Open Forum Infect. Dis.* **2020**, *7*, ofaa387.
(2) Gorbalenya, A. E.; Baker, S. C.; Baric, R. S.; de Groot, R. J.; Drosten, C.; Gulyaeva, A. A.; Haagmans, B. L.; Lauber, C.; Leontovich, A. M.; Neuman, B. W.; Penzar, D.; Perlman, S.; Poon, L. L. M.; Samborskiy, D. V.; Sidorov, I. A.; Sola, I.; Ziebuhr, J. Coronaviridae Study Group of the International Committee on Taxonomy of, V. The Species Severe Acute Respiratory Syndrome-related Coronavirus: Classifying 2019-nCoV and Naming it SARS-CoV-2. *Nat. Microbiol.* **2020**, *5*, 536−544.
(3) Corman, V. M.; Landt, O.; Kaiser, M.; Molenkamp, R.; Meijer, A.; Chu, D. K. W.; Bleicker, T.; Brünink, S.; Schneider, J.; Schmidt, M. L.; Mulders, D. G. J. C.; Haagmans, B. L.; van der Veer, B.; van den Brink, S.; Wijsman, L.; Goderski, G.; Romette, J.-L.; Ellis, J.; Zambon, M.; Peiris, M.; Goossens, H.; Reusken, C.; Koopmans, M. P. G.; Drosten, C. Detection of 2019 Novel Coronavirus (2019-nCoV) by Real-Time RT-PCR. *Eurosurveillance* **2020**, *25*, 2000045.
(4) Wang, X.; Yao, H.; Xu, X.; Zhang, P.; Zhang, M.; Shao, J.; Xiao, Y.; Wang, H. Limits of Detection of 6 Approved RT−PCR Kits for the Novel SARS-Coronavirus-2 (SARS-CoV-2). *Clin. Chem.* **2020**, *66*, 977−979.
(5) Huang, W. E.; Lim, B.; Hsu, C.-C.; Xiong, D.; Wu, W.; Yu, Y.; Jia, H.; Wang, Y.; Zeng, Y.; Ji, M.; Chang, H.; Zhang, X.; Wang, H.; Cui, Z. RT-LAMP for Rapid Diagnosis of Coronavirus SARS-CoV-2. *Microb. Biotechnol.* **2020**, *13*, 950−961.
(6) Broughton, J. P.; Deng, X.; Yu, G.; Fasching, C. L.; Servellita, V.; Singh, J.; Miao, X.; Streithorst, J. A.; Granados, A.; Sotomayor-Gonzalez, A.; Zorn, K.; Gopez, A.; Hsu, E.; Gu, W.; Miller, S.; Pan, C.-Y.; Guevara, H.; Wadford, D. A.; Chen, J. S.; Chiu, C. Y. CRISPR−Cas12-Based Detection of SARS-CoV-2. *Nat. Biotechnol.* **2020**, *38*, 870−874.
(7) Zhou, Y.; Wu, Y.; Ding, L.; Huang, X.; Xiong, Y. Point-of-Care COVID-19 Diagnostics Powered by Lateral Flow Assay. *TrAC, Trends Anal. Chem.* **2021**, *145*, 116452−116452.
(8) Mak, G. C. K.; Cheng, P. K. C.; Lau, S. S. Y.; Wong, K. K. Y.; Lau, C. S.; Lam, E. T. K.; Chan, R. C. W.; Tsang, D. N. C. Evaluation of Rapid Antigen Test for Detection of SARS-CoV-2 Virus. *J. Clin. Virol.* **2020**, *129*, 104500−104500.
(9) Guglielmi, G. Fast Coronavirus Tests: What They Can and Can't Do. *Nature* **2020**, *585*, 496−498.
(10) Bhalla, N.; Pan, Y.; Yang, Z.; Payam, A. F. Opportunities and Challenges for Biosensors and Nanoscale Analytical Tools for Pandemics: COVID-19. *ACS Nano* **2020**, *14*, 7783−7807.
(11) Chaibun, T.; Puenpa, J.; Ngamdee, T.; Boonapatcharoen, N.; Athamanolap, P.; O'Mullane, A. P.; Vongpunsawad, S.; Poovorawan, Y.; Lee, S. Y.; Lertanantawong, B. Rapid Electrochemical Detection of Coronavirus SARS-CoV-2. *Nat. Commun.* **2021**, *12*, 802.
(12) Torrente-Rodríguez, R. M.; Lukas, H.; Tu, J.; Min, J.; Yang, Y.; Xu, C.; Rossiter, H. B.; Gao, W. SARS-CoV-2 RapidPlex: A Graphene-Based Multiplexed Telemedicine Platform for Rapid and Low-Cost COVID-19 Diagnosis and Monitoring. *Matter* **2020**, *3*, 1981−1998.
(13) Li, J.; Lillehoj, P. B. Microfluidic Magneto Immunosensor for Rapid, High Sensitivity Measurements of SARS-CoV-2 Nucleocapsid Protein in Serum. *ACS Sens.* **2021**, *6*, 1270−1278.

(14) Seo, G.; Lee, G.; Kim, M. J.; Baek, S.-H.; Choi, M.; Ku, K. B.; Lee, C.-S.; Jun, S.; Park, D.; Kim, H. G.; Kim, S.-J.; Lee, J.-O.; Kim, B. T.; Park, E. C.; Kim, S. I. Rapid Detection of COVID-19 Causative Virus (SARS-CoV-2) in Human Nasopharyngeal Swab Specimens Using Field-Effect Transistor-Based Biosensor. *ACS Nano* **2020**, *14*, 5135−5142.
(15) Shao, W.; Shurin, M. R.; Wheeler, S. E.; He, X.; Star, A. Rapid Detection of SARS-CoV-2 Antigens Using High-Purity Semiconducting Single-Walled Carbon Nanotube-Based Field-Effect Transistors. *ACS Appl. Mater. Interfaces* **2021**, *13*, 10321−10327.
(16) Bong, J.-H.; Kim, T.-H.; Jung, J.; Lee, S. J.; Sung, J. S.; Lee, C. K.; Kang, M.-J.; Kim, H. O.; Pyun, J.-C. Pig Sera-derived Anti-SARS-CoV-2 Antibodies in Surface Plasmon Resonance Biosensors. *BioChip J.* **2020**, *14*, 358−368.
(17) Huang, J. C.; Chang, Y.-F.; Chen, K.-H.; Su, L.-C.; Lee, C.-W.; Chen, C.-C.; Chen, Y.-M. A.; Chou, C. Detection of Severe Acute Respiratory Syndrome (SARS) Coronavirus Nucleocapsid Protein in Human Serum Using a Localized Surface Plasmon Coupled Fluorescence Fiber-Optic Biosensor. *Biosens. Bioelectron.* **2009**, *25*, 320−325.
(18) Lichtenberg, J. Y.; Ling, Y.; Kim, S. Non-Specific Adsorption Reduction Methods in Biosensing. *Sensors* **2019**, *19*, 2488.
(19) Jiang, C.; Wang, G.; Hein, R.; Liu, N.; Luo, X.; Davis, J. J. Antifouling Strategies for Selective In Vitro and In Vivo Sensing. *Chem. Rev.* **2020**, 3852.
(20) Blaszykowski, C.; Sheikh, S.; Thompson, M. A Survey of State-of-the-Art Surface Chemistries to Minimize Fouling from Human and Animal Biofluids. *Biomater. Sci.* **2015**, *3*, 1335−1370.
(21) Maan, A. M. C.; Hofman, A. H.; de Vos, W. M.; Kamperman, M. Recent Developments and Practical Feasibility of Polymer-Based Antifouling Coatings. *Adv. Funct. Mater.* **2020**, *30*, 2000936.
(22) Mitra, D.; Kang, E.-T.; Neoh, K. G. Polymer-Based Coatings with Integrated Antifouling and Bactericidal Properties for Targeted Biomedical Applications. *ACS Appl. Polym. Mater.* **2021**, *3*, 2233−2263.
(23) Asha, A. B.; Chen, Y.; Narain, R. Bioinspired Dopamine and Zwitterionic Polymers for Non-Fouling Surface Engineering. *Chem. Soc. Rev.* **2021**, *50*, 11668−11683.
(24) Vaisocherová, H.; Brynda, E.; Homola, J. Functionalizable Low-Fouling Coatings for Label-Free Biosensing in Complex Biological Media: Advances and Applications. *Anal. Bioanal. Chem.* **2015**, *407*, 3927−3953.
(25) Anthi, J.; Kolivoška, V.; Holubová, B.; Vaisocherová-Lísalová, H. Probing Polymer Brushes with Electrochemical Impedance Spectroscopy: A Mini Review. *Biomater. Sci.* **2021**, 7379.
(26) Shiddiky, M. J. A.; Kithva, P. H.; Kozak, D.; Trau, M. An Electrochemical Immunosensor to Minimize the Nonspecific Adsorption and to Improve Sensitivity of Protein Assays in Human Serum. *Biosens. Bioelectron.* **2012**, *38*, 132−137.
(27) Riedel, T.; Hageneder, S.; Surman, F.; Pop-Georgievski, O.; Noehammer, C.; Hofner, M.; Brynda, E.; Rodriguez-Emmenegger, C.; Dostálek, J. Plasmonic Hepatitis B Biosensor for the Analysis of Clinical Saliva. *Anal. Chem.* **2017**, *89*, 2972−2977.
(28) Yang, W.; Xue, H.; Carr, L. R.; Wang, J.; Jiang, S. Zwitterionic Poly(carboxybetaine) Hydrogels for Glucose Biosensors in Complex Media. *Biosens. Bioelectron.* **2011**, *26*, 2454−2459.
(29) Chou, Y.-N.; Sun, F.; Hung, H.-C.; Jain, P.; Sinclair, A.; Zhang, P.; Bai, T.; Chang, Y.; Wen, T.-C.; Yu, Q.; Jiang, S. Ultra-Low Fouling and High Antibody Loading Zwitterionic Hydrogel Coatings for Sensing and Detection in Complex Media. *Acta Biomater.* **2016**, *40*, 31−37.
(30) Vaisocherová-Lísalová, H.; Surman, F.; Víšová, I.; Vala, M.; Špringer, T.; Ermini, M. L.; Šípová, H.; Šedivák, P.; Houska, M.; Riedel, T.; Pop-Georgievski, O.; Brynda, E.; Homola, J. Copolymer Brush-Based Ultralow-Fouling Biorecognition Surface Platform for Food Safety. *Anal. Chem.* **2016**, *88*, 10533−10539.
(31) Liu, B.; Liu, X.; Shi, S.; Huang, R.; Su, R.; Qi, W.; He, Z. Design and Mechanisms of Antifouling Materials for Surface Plasmon Resonance Sensors. *Acta Biomater.* **2016**, *40*, 100−118.
(32) Víšová, I.; Vrabcová, M.; Forinová, M.; Zhigunová, Y.; Mironov, V.; Houska, M.; Bittrich, E.; Eichhorn, K.-J.; Hashim, H.; Schovánek, P.; Dejneka, A.; Vaisocherová-Lisalová, H. Surface Preconditioning Influences the Antifouling Capabilities of Zwitterionic and Nonionic Polymer Brushes. *Langmuir* **2020**, *36*, 8485−8493.
(33) Lísalová, H.; Brynda, E.; Houska, M.; Víšová, I.; Mrkvová, K.; Song, X. C.; Gedeonová, E.; Surman, F.; Riedel, T.; Pop-Georgievski, O.; Homola, J. Ultralow-Fouling Behavior of Biorecognition Coatings Based on Carboxy-Functional Brushes of Zwitterionic Homo- and Copolymers in Blood Plasma: Functionalization Matters. *Anal. Chem.* **2017**, *89*, 3524−3531.
(34) Vaisocherová, H.; Šípová, H.; Víšová, I.; Bocková, M.; Špringer, T.; Ermini, M. L.; Song, X.; Krejčík, Z.; Chrastinová, L.; Pastva, O.; Pimková, K.; Merkerová, M. D.; Dyr, J. E.; Homola, J. Rapid and Sensitive Detection of Multiple MicroRNAs in Cell Lysate by Low-Fouling Surface Plasmon Resonance Biosensor. *Biosens. Bioelectron.* **2015**, *70*, 226−231.
(35) Pandey, L. M. Design of Engineered Surfaces for Prospective Detection of SARS-CoV-2 Using Quartz Crystal Microbalance-Based Techniques. *Expert Rev. Proteomics* **2020**, *17*, 425−432.
(36) Chang, C.-k.; Hou, M.-H.; Chang, C.-F.; Hsiao, C.-D.; Huang, T.-h. The SARS Coronavirus Nucleocapsid Protein − Forms and Functions. *Antiviral Res.* **2014**, *103*, 39−50.
(37) Davidson, A. D.; Williamson, M. K.; Lewis, S.; Shoemark, D.; Carroll, M. W.; Heesom, K. J.; Zambon, M.; Ellis, J.; Lewis, P. A.; Hiscox, J. A.; Matthews, D. A. Characterisation of the Transcriptome and Proteome of SARS-CoV-2 Reveals A Cell Passage Induced In-Frame Deletion of the Furin-Like Cleavage Site from the Spike Glycoprotein. *Genome Med.* **2020**, *12*, 68−68.
(38) Kim, D.; Lee, J.-Y.; Yang, J.-S.; Kim, J. W.; Kim, V. N.; Chang, H. The Architecture of SARS-CoV-2 Transcriptome. *Cell* **2020**, *181*, 914−921.e10.
(39) Bojkova, D.; Klann, K.; Koch, B.; Widera, M.; Krause, D.; Ciesek, S.; Cinatl, J.; Münch, C. Proteomics of SARS-CoV-2-Infected Host Cells Reveals Therapy Targets. *Nature* **2020**, *583*, 469−472.
(40) Dai, L.; Gao, G. F. Viral Targets for Vaccines against COVID-19. *Nat. Rev. Immunol.* **2021**, *21*, 73−82.
(41) De Gasparo, R.; Pedotti, M.; Simonelli, L.; Nickl, P.; Muecksch, F.; Cassaniti, I.; Percivalle, E.; Lorenzi, J. C. C.; Mazzola, F.; Magrì, D.; Michalcikova, T.; Haviernik, J.; Honig, V.; Mrazkova, B.; Polakova, N.; Fortova, A.; Tureckova, J.; Iatsiuk, V.; Di Girolamo, S.; Palus, M.; Zudova, D.; Bednar, P.; Bukova, I.; Bianchini, F.; Mehn, D.; Nencka, R.; Strakova, P.; Pavlis, O.; Rozman, J.; Gioria, S.; Sammartino, J. C.; Giardina, F.; Gaiarsa, S.; Pan-Hammarström, Q.; Barnes, C. O.; Bjorkman, P. J.; Calzolai, L.; Piralla, A.; Baldanti, F.; Nussenzweig, M. C.; Bieniasz, P. D.; Hatziioannou, T.; Prochazka, J.; Sedlacek, R.; Robbiani, D. F.; Ruzek, D.; Varani, L. Bispecific IgG Neutralizes SARS-CoV-2 Variants and Prevents Escape in Mice. *Nature* **2021**, *593*, 424−428.
(42) Hansen, J.; Baum, A.; Pascal, K. E.; Russo, V.; Giordano, S.; Wloga, E.; Fulton, B. O.; Yan, Y.; Koon, K.; Patel, K.; Chung, K. M.; Hermann, A.; Ullman, E.; Cruz, J.; Rafique, A.; Huang, T.; Fairhurst, J.; Libertiny, C.; Malbec, M.; Lee, W.-y.; Welsh, R.; Farr, G.; Pennington, S.; Deshpande, D.; Cheng, J.; Watty, A.; Bouffard, P.; Babb, R.; Levenkova, N.; Chen, C.; Zhang, B.; Romero Hernandez, A.; Saotome, K.; Zhou, Y.; Franklin, M.; Sivapalasingam, S.; Lye, D. C.; Weston, S.; Logue, J.; Haupt, R.; Frieman, M.; Chen, G.; Olson, W.; Murphy, A. J.; Stahl, N.; Yancopoulos, G. D.; Kyratsous, C. A. Studies in Humanized Mice and Convalescent Humans Yield a SARS-CoV-2 Antibody Cocktail. *Science* **2020**, *369*, 1010−1014.
(43) Baum, A.; Fulton, B. O.; Wloga, E.; Copin, R.; Pascal, K. E.; Russo, V.; Giordano, S.; Lanza, K.; Negron, N.; Ni, M.; Wei, Y.; Atwal, G. S.; Murphy, A. J.; Stahl, N.; Yancopoulos, G. D.; Kyratsous, C. A. Antibody Cocktail to SARS-CoV-2 Spike Protein Prevents Rapid Mutational Escape Seen with Individual Antibodies. *Science* **2020**, *369*, 1014−1018.
(44) Grifoni, A.; Sidney, J.; Zhang, Y.; Scheuermann, R. H.; Peters, B.; Sette, A. A Sequence Homology and Bioinformatic Approach Can

https://doi.org/10.1021/acsami.1c16930
ACS Appl. Mater. Interfaces 2021, 13, 60612−60624

Predict Candidate Targets for Immune Responses to SARS-CoV-2. *Cell Host Microbe* **2020**, *27*, 671−680.e2.
(45) Bullard, J.; Dust, K.; Funk, D.; Strong, J. E.; Alexander, D.; Garnett, L.; Boodman, C.; Bello, A.; Hedley, A.; Schiffman, Z.; Doan, K.; Bastien, N.; Li, Y.; Van Caeseele, P. G.; Poliquin, G. Predicting Infectious Severe Acute Respiratory Syndrome Coronavirus 2 from Diagnostic Samples. *Clin. Infect. Dis.* **2020**, *71*, 2663−2666.
(46) Vandenberg, O.; Martiny, D.; Rochas, O.; van Belkum, A.; Kozlakidis, Z. Considerations for Diagnostic COVID-19 Tests. *Nat. Rev. Microbiol.* **2021**, *19*, 171−183.
(47) Nalla, A. K.; Casto, A. M.; Huang, M.-L. W.; Perchetti, G. A.; Sampoleo, R.; Shrestha, L.; Wei, Y.; Zhu, H.; Jerome, K. R.; Greninger, A. L. Comparative Performance of SARS-CoV-2 Detection Assays Using Seven Different Primer-Probe Sets and One Assay Kit. *J. Clin. Microbiol.* **2020**, *58*, 1−6.
(48) Weissleder, R.; Lee, H.; Ko, J.; Pittet, M. J. COVID-19 Diagnostics in Context. *Sci. Transl. Med.* **2020**, *12*, eabc1931−eabc1931.
(49) Woloshin, S.; Patel, N.; Kesselheim, A. S. False Negative Tests for SARS-CoV-2 Infection — Challenges and Implications. *N. Engl. J. Med.* **2020**, *383*, e38−e38.
(50) Chirathaworn, C.; Sripramote, M.; Chalongviriyalert, P.; Jirajariyavej, S.; Kiatpanabhikul, P.; Saiyarin, J.; Soudon, C.; Thienfaidee, O.; Palakawong Na Ayuthaya, T.; Brukesawan, C.; Chaiwanichsiri, D.; Intharasongkroh, D.; Wanlapakorn, N.; Chansaenroj, J.; Puenpa, J.; Yorsaeng, R.; Thitithanyanont, A.; Kitphati, R.; Mungaomklang, A.; Nagavajara, P.; Poovorawan, Y. SARS-CoV-2 RNA Shedding in Recovered COVID-19 Cases and the Presence of Antibodies against SARS-CoV-2 in Recovered COVID-19 Cases and Close Contacts, Thailand, April-June 2020. *PLoS One* **2020**, *15*, e0236905−e0236905.
(51) Vetter, P.; Eberhardt, C. S.; Meyer, B.; Martinez Murillo, P. A.; Torriani, G.; Pigny, F.; Lemeille, S.; Cordey, S.; Laubscher, F.; Vu, D.-L.; Calame, A.; Schibler, M.; Jacquerioz, F.; Blanchard-Rohner, G.; Siegrist, C.-A.; Kaiser, L.; Didierlaurent, A. M.; Eckerle, I. Daily Viral Kinetics and Innate and Adaptive Immune Response Assessment in COVID-19: a Case Series. *mSphere* **2020**, *5*, 1−35.
(52) Avanzato, V. A.; Matson, M. J.; Seifert, S. N.; Pryce, R.; Williamson, B. N.; Anzick, S. L.; Barbian, K.; Judson, S. D.; Fischer, E. R.; Martens, C.; Bowden, T. A.; de Wit, E.; Riedo, F. X.; Munster, V. J. Case Study: Prolonged Infectious SARS-CoV-2 Shedding from an Asymptomatic Immunocompromised Individual with Cancer. *Cell* **2020**, *183*, 1901−1912.e9.
(53) Porte, L.; Legarraga, P.; Vollrath, V.; Aguilera, X.; Munita, J. M.; Araos, R.; Pizarro, G.; Vial, P.; Iruretagoyena, M.; Dittrich, S.; Weitzel, T. Evaluation of a Novel Antigen-Based Rapid Detection Test for The Diagnosis of SARS-CoV-2 in Respiratory Samples. *Int. J. Infect. Dis.* **2020**, *99*, 328−333.
(54) Weitzel, T.; Legarraga, P.; Iruretagoyena, M.; Pizarro, G.; Vollrath, V.; Araos, R.; Munita, J. M.; Porte, L. Comparative Evaluation of Four Rapid SARS-CoV-2 Antigen Detection Tests Using Universal Transport Medium. *Travel Med. Infect. Dis.* **2021**, *39*, 101942−101942.
(55) Alafeef, M.; Dighe, K.; Moitra, P.; Pan, D. Rapid, Ultrasensitive, and Quantitative Detection of SARS-CoV-2 Using Antisense Oligonucleotides Directed Electrochemical Biosensor Chip. *ACS Nano* **2020**, *14*, 17028−17045.
(56) Raziq, A.; Kidakova, A.; Boroznjak, R.; Reut, J.; Öpik, A.; Syritski, V. Development of a Portable MIP-Based Electrochemical Sensor for Detection of SARS-CoV-2 Antigen. *Biosens. Bioelectron.* **2021**, *178*, 113029.
(57) de Lima, L. F.; Ferreira, A. L.; Torres, M. D. T.; de Araujo, W. R.; de la Fuente-Nunez, C. Minute-Scale Detection of SARS-CoV-2 Using a Low-Cost Biosensor Composed of Pencil Graphite Electrodes. *Proc. Natl. Acad. Sci. U. S. A.* **2021**, *118*, No. e2106724118.
(58) Fabiani, L.; Saroglia, M.; Galatà, G.; De Santis, R.; Fillo, S.; Luca, V.; Faggioni, G.; D'Amore, N.; Regalbuto, E.; Salvatori, P.; Terova, G.; Moscone, D.; Lista, F.; Arduini, F. Magnetic Beads Combined with Carbon Black-Based Screen-Printed Electrodes for COVID-19: A Reliable and Miniaturized Electrochemical Immunosensor for SARS-CoV-2 Detection in Saliva. *Biosens. Bioelectron.* **2021**, *171*, 112686−112686.
(59) Víšová, I.; Smolková, B.; Uzhytchak, M.; Vrabcová, M.; Zhigunova, Y.; Houska, M.; Surman, F.; de Los Santos Pereira, A.; Lunov, O.; Dejneka, A.; Vaisocherová-Lísalová, H. Modulation of Living Cell Behavior with Ultra-Low Fouling Polymer Brush Interfaces. *Macromol. Biosci.* **2020**, *20*, No. e1900351.
(60) Chen, H.-S.; Hou, S.-C.; Jian, J.-W.; Goh, K.-S.; Shen, S.-T.; Lee, Y.-C.; You, J.-J.; Peng, H.-P.; Kuo, W.-C.; Chen, S.-T.; Peng, M.-C.; Wang, A. H. J.; Yu, C.-M.; Chen, I.-C.; Tung, C.-P.; Chen, T.-H.; Ping Chiu, K.; Ma, C.; Yuan Wu, C.; Lin, S.-W.; Yang, A.-S. Predominant Structural Configuration of Natural Antibody Repertoires Enables Potent Antibody Responses Against Protein Antigens. *Sci. Rep.* **2015**, *5*, 12411−12411.
(61) Jian, J.-W.; Chen, H.-S.; Chiu, Y.-K.; Peng, H.-P.; Tung, C.-P.; Chen, I.-C.; Yu, C.-M.; Tsou, Y.-L.; Kuo, W.-Y.; Hsu, H.-J.; Yang, A.-S. Effective Binding to Protein Antigens by Antibodies from Antibody Libraries Designed with Enhanced Protein Recognition Propensities. *mAbs* **2019**, *11*, 373−387.
(62) Hou, S.-C.; Chen, H.-S.; Lin, H.-W.; Chao, W.-T.; Chen, Y.-S.; Fu, C.-Y.; Yu, C.-M.; Huang, K.-F.; Wang, A. H. J.; Yang, A.-S. High Throughput Cytotoxicity Screening of Anti-HER2 Immunotoxins Conjugated with Antibody Fragments from Phage-Displayed Synthetic Antibody Libraries. *Sci. Rep.* **2016**, *6*, 31878−31878.
(63) Tung, C.-P.; Chen, I.-C.; Yu, C.-M.; Peng, H.-P.; Jian, J.-W.; Ma, S.-H.; Lee, Y.-C.; Jan, J.-T.; Yang, A.-S. Discovering Neutralizing Antibodies Targeting the Stem Epitope of H1N1 Influenza Hemagglutinin with Synthetic Phage-Displayed Antibody Libraries. *Sci. Rep.* **2015**, *5*, 15053−15053.
(64) De Madrid, A. T.; Porterfield, J. S. A Simple Micro-Culture Method for the Study of Group B Arboviruses. *Bull. W. H. O.* **1969**, *40*, 113−121.
(65) Alexander, M. R.; Rootes, C. L.; van Vuren, P. J.; Stewart, C. R. Concentration of Infectious SARS-CoV-2 by Polyethylene Glycol Precipitation. *J. Virol. Methods* **2020**, *286*, 113977−113977.
(66) Wessel, D.; Flügge, U. I. A Method for the Quantitative Recovery of Protein in Dilute Solution in the Presence of Detergents and Lipids. *Anal. Biochem.* **1984**, *138*, 141−143.
(67) Rappsilber, J.; Mann, M.; Ishihama, Y. Protocol for Micro-Purification, Enrichment, Pre-Fractionation and Storage of Peptides for Proteomics Using StageTips. *Nat. Protoc.* **2007**, *2*, 1896−1906.
(68) Cox, J.; Mann, M. MaxQuant Enables High Peptide Identification Rates, Individualized p.p.b.-Range Mass Accuracies and Proteome-Wide Protein Quantification. *Nat. Biotechnol.* **2008**, *26*, 1367−1372.
(69) Tyanova, S.; Cox, J. Perseus: A Bioinformatics Platform for Integrative Analysis of Proteomics Data in Cancer Research. *Methods Mol. Biol.* **2018**, *1711*, 133−148.

https://doi.org/10.1021/acsami.1c16930
ACS Appl. Mater. Interfaces 2021, 13, 60612−60624